Porous aligned ZnSr-doped β-TCP/silk fibroin scaffolds using ice-templating method for bone tissue engineering applications

D. Bicho[1,2], R.F. Canadas[1,2], C. Gonçalves[1,2], S. Pina[1,2], R.L. Reis[1,2] and J.M. Oliveira[1,2,+]

[1] 3B's Research Group, I3Bs – Research Institute on Biomaterials, Biodegradables and Biomimetics, University of Minho, Headquarters of the European Institute of Excellence on Tissue Engineering and Regenerative Medicine, AvePark, Parque de Ciência e Tecnologia, Zona Industrial da Gandra, 4805-017 Barco, Guimarães, Portugal;

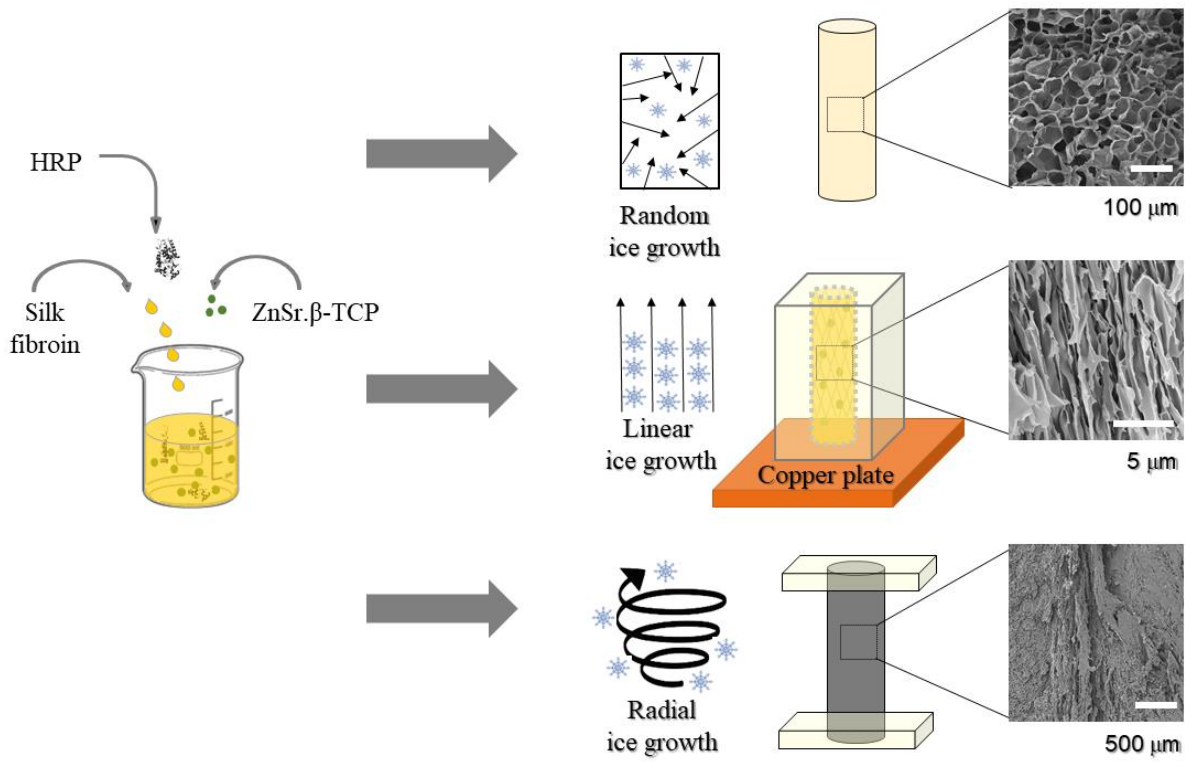[2] ICVS/3B's - PT Government Associate Laboratory, Braga/Guimarães, Portugal;

[+] Corresponding author: J.M. Oliveira: miguel.oliveira@i3bs.uminho.pt

Abstract

The bone is a complex and dynamic structure subjected to constant stress and remodeling. Due to the worldwide incidence of bone disorders, tissue scaffolds and engineered bone tissues have emerged as solutions for bone grafting, which require sophisticated scaffolding architectures while keeping high mechanical performance. However, the conjugation of a bone-like scaffold architecture with efficient mechanical properties is still a critical challenge for biomedical applications. In this sense, the present study focused on the modulating the architecture of silk fibroin (SF) scaffolds crosslinked with horseradish peroxidase and mixed with zinc (Zn) and strontium (Sr)-doped β-tricalcium phosphate (ZnSr.TCP) to mimic bone structures. The ZnSr.TCP-SF hydrogels were tuned by programmable ice-templating parameters, and further freeze-dried, in order to obtain 3D scaffolds with controlled pore orientation. The results showed interconnected channels in the ZnSr.TCP-SF scaffolds that mimic the porous network of the native subchondral bone matrix. The architecture of the scaffolds was characterized by microCT, showing tunable pore size according to freezing temperatures (-196 ℃: ~80.2 ± 20.5 µm; -80 ℃: ~73.1 ± 20.5 µm; -20 ℃: ~104.7 ± 33.7 µm). The swelling ratio, weight loss, and rheological properties were also assessed, revealing efficient scaffold integrity and morphology after aqueous immersion. Thus, the ZnSr.TCP-SF scaffolds made of aligned porous structure were developed as affordable candidates for future applications in clinical osteoregeneration and *in vitro* bone tissue modelling.

Keywords: ZnSr-doped β-tricalcium phosphate, silk fibroin, ice-templating, pore alignment, scaffolds, bone tissue engineering.

35 **Graphical abstract**

Random ice growth — 100 μm

Linear ice growth — Copper plate — 5 μm

Radial ice growth — 500 μm

36

1. Introduction

Throughout the last decades, a noteworthy amount of research has headed in the direction of constructing well-defined structures that mimic the alignment of the extracellular matrix (ECM) to provide enhanced guidance cues, thus improving cell alignment, phenotype, and metabolic activity[1]. To meet these unique features, tissue-engineering (TE) scaffolds with defined matrix orientation have been developed to mimic several natural hierarchically instructed architectures, such as bone, cartilage, tendon, muscle, among others.[2–4]

Depending on the nature of bone, several densities, compositions, pore sizes, and orientations of the artificial matrices fibers are required to mimic the tissue. Therefore, the challenge lies on its structural heterogeneity because even though bone tissue is divided into two categories, these are structurally and mechanically distinct. Specifically, the trabecular bone (e.g, head of the femur), presents a spongy-like structure (random) followed by a radial gradient one, which corresponds to the cortical bone, and a more aligned porous architecture up to the cancellous bone (e.g. shaft of the femur). Structurally, cortical bones are highly dense and present low porosity (5 - 30%), while cancellous bones are highly porous (50 - 90%).[5,6] For example, in long bone structures, as the case of the femur, hollow cylinders are present at the end of the cortical bone. These are called osteons and are composed of collagen fibers inserted in hydroxyapatite (HAp) crystals.[7]

Bone ECM, among other molecules, contains 99% of the body's calcium mostly in the form of HAp with trace elements replacing hydroxyl and phosphate groups.[8] Several attempts to prepare TE scaffolds with the same composition as the native bone ECM have been made, and some have actually been FDA-approved (e.g., Collagraft®, Healos®, Mozaik® and Ossimend®). Collagen and HAp composites appealed some interest specifically because the ductility of collagen which helps to decrease the brittleness of HAp while keeping its biocompatibility and osteogenic capacity.[9] However, collagen has also some limitations, namely a quick degradation, low compression strength and modulus, which impacts its use on hard bone tissue with slow regeneration rate.[10]

Presently, the use of β-tricalcium phosphate (TCP) has been preferred over HAp, due to its faster degradation,[10] and resorbability, as well as, the promotion of bone ingrowth's through osteoconduction.[11,12] Additionally, TCP can be doped with several ions to enhance the mechanical strength, osteogenic and neovascularization potential (e.g. Sr^{2+},Zn^{2+}) of the scaffolds.[13–15] The combination of inorganic materials and biopolymers such as, TCP and SF respectively, has resulted in composite structures with improved mechanical and biological performance for TE.[16–18]

SF is the structural protein extracted from the *Bombyx mori* silkworm cocoon, that represents one of the most robust and available biopolymers in nature. It has been applied in the biomedical field due to its biodegradability, non-cytotoxicity, and physiological properties.[19,20] Using horseradish peroxidase (HRP) and hydrogen peroxide (H_2O_2), it is possible to covalently crosslink SF

74 improving the strength, toughness, elasticity and mechanical tunability of the scaffolds, while

75 enabling the control over degradation rates.[16,18,21–23] This biopolymer can be potentially useful in

76 osteogenic regeneration due to its resemblance to collagen type I. Specifically, the anionic nature

77 of the β-sheet structures of SF act as nucleation sites for the deposition of HAp nanocrystals.[23,24]

78 These characteristics fulfill the requirements to create matrices as bone substitutes with efficient

79 mechanical characteristics to avoid crushing under physiological loads.

80 To achieve an organization that mimics the native bone, several techniques have been applied

81 including the foam replica method, gas foaming, phase separation, rapid prototyping,

82 electrospinning and molecular self-assembly. Yet, those methods are limited due to their complex

83 fabrication steps, production of toxic chemicals, severe processing conditions, and difficulty in

84 mimicking the oriented internal structure of some natural tissues.[25] Therefore, a more versatile

85 technique to produce 3D matrices named ice-templating has been explored[26]. Ice-templating does

86 not require chemical processing, allowing not only to control the direction of growth and size of

87 the ice crystals, but also to induce pore directionality in function of the temperature gradient

88 creating linear, radial, and/or random networks.[27,28]

89 Considering the great biological performance of the above-mentioned composite materials, it was

90 our aim to design specific micro-architectures through ice-templating mimicking the bone

91 structure, using the same composition based on SF combined with TCP doped with ZnSr. This

92 eco-friendly, scalable, and cost-effective technique was applied to induce unique linear and radial

93 porous architectures by means of varying the mold composition and directionality of the ice

94 nucleation at three different temperatures: -196 ℃; -80 ℃ and -20 ℃. In this sense, the

95 morphology, pore orientation, pore size, porosity amount, and rheological properties of the

96 scaffolds were investigated. The ZnSr.TCP-SF scaffolds were also evaluated in terms of swelling

97 ratio and weight loss.

98

2. Materials and methods

2.1 Preparation of ZnSr-doped β-tricalcium phosphate

101 β-TCP powders doped with 10 mol.% of Sr^{2+} + Zn^{2+} (regarding the Sr^{2+} + Zn^{2+} and Ca^{2+} molar

102 ratio) (ZnSr.TCP) were synthesized by wet chemical precipitation according to a previous

103 method.[17] Briefly, diammonium hydrogen phosphate ($[NH_4]_2HPO_4$, Sigma-Aldrich, MO, USA)

104 solution was dropped into calcium nitrate tetrahydrate ($Ca[NO_3]_2·4H_2O$, Sigma-Aldrich, MO,

105 USA) solution containing strontium nitrate ($Sr[NO_3]$, Sigma-Aldrich, MO, USA) and zinc nitrate

106 ($Zn[NO_3]_2·6H_2O$, Sigma-Aldrich, MO, USA), in a molar ratio of $(Ca + X)/P = 1.48$ (where X

107 corresponds to Sr + Zn). The mixture was kept in a reactor at 30 ℃ with continuous stirring for 4

108 h and ripened for further 20 h under rest conditions, at pH value ~ 7, by adjusting with required

109 amounts of 8 M NH_4OH solution. The resulting precipitates were vacuum filtered, dried at 100

110   °C, and heat-treated for 2 h at 1100 °C. Afterwards, the powders were milled and sieved (mesh

111   size: 36 μm).

112

113   *2.2 Preparation of Sil Fibroin solution*

114   *Bombyx mori* cocoons (from the Portuguese Association of Parents and Friends of Mentally

115   Disabled Citizens, Castelo Branco, Portugal) were used to extract SF according to the previously

116   reported protocol.[29] To begin, the cocoons were boiled in 0.02 M sodium carbonate solution

117   (Sigma-Aldrich, MO, USA) for 1 h to extract the SF. Then, the purified SF was dissolved in 9.3

118   M lithium bromide solution (Sigma-Aldrich, MO, USA) at 70 °C for 1 h, and dialyzed in distilled

119   water for 2 d using benzoylated dialysis tubing (MWCO 2000 from Sigma-Aldrich, MO, USA)

120   to remove residual lithium bromide. Finally, poly(ethylene glycol) (Sigma-Aldrich MO, USA)

121   was added to SF to yield a solution of 8% (w/v), which was determined by weighing the wet and

122   dry mass of the prepared SF solution.

123

124   *2.3 Fabrication of ZnSr-doped β-TCP-SF composite scaffolds*

125   The present work allowed to optimize the best conditions to prepare anisotropic structures

126   for osteogenic regeneration as previously reported.[30] Accordingly, the optimal composite

127   hydrogels were obtained with a blend ratio of 95/5 (w/v) of enzymatically induced SF and

128   ZnSr.TCP powder. For that, ZnSr.TCP-SF scaffolds were prepared by mixing 1 mL of SF solution

129   (concentrated at 8% (w/v)), 50 μL of horseradish peroxidase solution (HRP type VI, 0.84 mg/mL),

130   and 65 μL hydrogen peroxide solution (H_2O_2, 0.36% (w/v), Panreac, Barcelona, Spain), and 5

131   wt.% ZnSr.TCP, in a water bath at 37 °C until complete gelation. Afterwards, the hydrogels were

132   frozen at –196 ºC, -80 °C or -20 ºC for 2 h, 4 h or overnight, respectively. The temperatures were

133   reached using either liquid nitrogen (-196 ºC) in a closed container or common laboratorial

134   freezers (-80 ° C and -20 ºC). The anisotropic linear structure was achieved with a plastic mold

135   press fit inside polystyrene foams to function as heat insulators, the styrofoam mold covered the

136   whole silicon tube except for the bottom, which contacted directly with the copper plate thus

137   promoting the ice crystals to grow over the main axis of the scaffolds (vertical growth) and

138   forming linear pores.[31,32] As previously referred, the first half of the scaffold, in direct contact

139   with the copper plate, was discarded to avoid a more compact structure.[31] On the other hand, the

140   radial structure required two thin pieces of insulating material in the top and bottom of a thermally

141   conductive metallic mold (aluminum), to ensure the lateral freezing of the structure and induce

142   the radial ice growth.[33,34] To obtain the isotropic (random) porosity no insulation was needed,

143   only the silicon tube was used in direct contact with the freezing environment allowing a non-

144   directional freezing and random orientation of the ice crystal (Figure 1A).[35] Finally, the frozen

145   structures were lyophilized (Telstar-Cryodos -80, Spain) for the period of 3 days.

146

147 *2.4 Physicochemical characterization of the scaffolds*

148 **2.4.1 X-rays micro-computed tomography (Micro-CT)**

149 The microstructure of the ZnSr.TCP-SF scaffolds was evaluated using a high-resolution X-ray

150 micro-computed tomography system (Skyscan 1272, scanner Bruker Micro-CT, Billerica, MA,

151 USA). Samples were scanned using a pixel size of 10 μm, and a rotation step of 0.45º over a

152 rotation range of 180º. The acquisitions were performed with an X-ray source fixed at 50 keV and

153 200 μA, with no filter. The images were acquired with 1632x1092 pixels, and binary images were

154 used for morphometric analysis (CT Analyzer v1.17.0.0, Bruker, Billerica, MA, USA) to quantify

155 the porosity, mean pore size and mean wall thickness. The cross-sectional images of the scaffolds

156 were also created, visualized and registered using the image processing and reconstruction

157 software CT-Vox (v3.3.0, Bruker, Billerica, MA, USA). All the experiments were performed in

158 replicates.

159

160 **2.4.2   Shape factors**

161

162 **2.4.3   Rheology**

163 Rheological analyses were performed using a Kinexus pro+rheometer (Malvern Instruments,

164 UK), using the acquisition software rSpace. The measuring system used in these experiments was

165 equipped with a stainless steel (316 grade) plate-plate system: the upper measurement geometry

166 with 8 mm of diameter and a plate lower pedestal, both with a rough finish to prevent slipping.

167 Oscillatory experiments were performed to study viscoelasticity, by obtaining frequency sweep

168 curves. All plots are obtained by the average of at least 3 experiments. These experiments were

169 conducted with the ZnSr.TCP-SF scaffolds obtained with 9 different conditions: random, linear

170 and radially oriented pores each one produced at -196 ºC, -80 ºC and -20 ºC, and then lyophilized.

171 The samples were rehydrated, in phosphate buffer saline (PBS) solution at 4 ºC, 24 h before the

172 rheological experiments.

173 The phase angle value can be obtained by using Equation 1:

174

175 $$\tan \delta = G'/G'' \qquad \text{(Equation 1)}$$

176

177 This equation describes the ratio between the loss (G'') and storage (G') modulus in a viscoelastic

178 material, that is defined as the phase angle (δ) tangent, which provides a measure of damping in

179 the material. The phase angle (δ) has values ranging between 0° to 90° for viscoelastic samples,

180 being higher than 45º for fluid state samples (90° only for ideally viscous flow, where the energy

181 dissipated as heat) and lower than 45º for gel-like state samples (0º only for ideally elastic

182 behavior where the energy is stored in the material). G' describes the elastic behavior (being

183 higher for solid samples) while G'' describes the viscous behavior (being higher for liquid
184 samples).[36]

185

186 **2.4.3 Swelling ratio**
187 The swelling ratio (SR) of the ZnSr.TCP-SF scaffolds were calculated in order to determine the
188 fractional increase in the weight due to water absorption. The SR was determined by hydrating
189 the scaffolds in PBS and then leaving them to swell for 48 h. SR was calculated according to
190 Equation 2:

191

192 $$SR = (W_x - W_1)/W_1 \qquad \text{(Equation 2)}$$

193

194 where, W_1 and W_x are the weight of the wet scaffolds and the weight after swelling at each time
195 point (0 h, 1 h, 6 h, 24 h, 48 h), respectively. The experiments were done in duplicates (n= 6).

196

197 **2.4.4 Stability of the scaffolds**
198 The stability of ZnSr.TCP-SF scaffolds was evaluated through weight loss evaluation. The wet
199 weight of the samples was registered in an analytical balance after 30 d of immersion in PBS at
200 37 °C. After this time, the samples were washed in distilled water three times and dried overnight
201 at 37 °C. The weights of the scaffolds before immersion was also measured (n=3). Afterwards,
202 the percentage of weight loss was calculated according to Equation 3:

203

204 $$WL \; (\%) = (m_f - m_i)/m_i * 100 \qquad \text{(Equation 3)}$$

205

206 where, m_i and m_f are the initial and final weight of the scaffolds.

207

208 **2.5. Statistical analysis**
209 Statistical analysis was executed using GraphPad Prism 8 version software (GraphPad Software,
210 La Jolla, CA, USA). Statistics using One- and Two-Way ANOVA multiple comparison were used
211 to compare between group. Statistical significances were determined as *$p<0.05$ and ** $p<0.01$.
212 All assays were performed in triplicates and values were reported as mean ± standard deviation
213 (SD).

214

215 **3. Results**
216 The present work tested the production of scaffolds with tunable architecture, based on
217 enzymatically-crosslinked SF combined with ZnSr-doped TCP composites, using the ice-
218 templating technique. After producing the composites, a freezing step in silicon, plastic, or
219 aluminum cylinders (Figure 1A) resulted in specific pore directionality, as random, linear, or

220 radial, respectively. The qualitative analysis of the ZnSr.TCP-SF scaffolds architecture was

221 performed using micro-CT, unveiling the pore orientation in the scaffolds longitudinal section, as

222 depicted in Figure 1B. The pore size decreased with temperature (from -20 ºC to -196 ºC), while

223 the pore orientation and density were increasingly defined, particularly at -196 ºC.
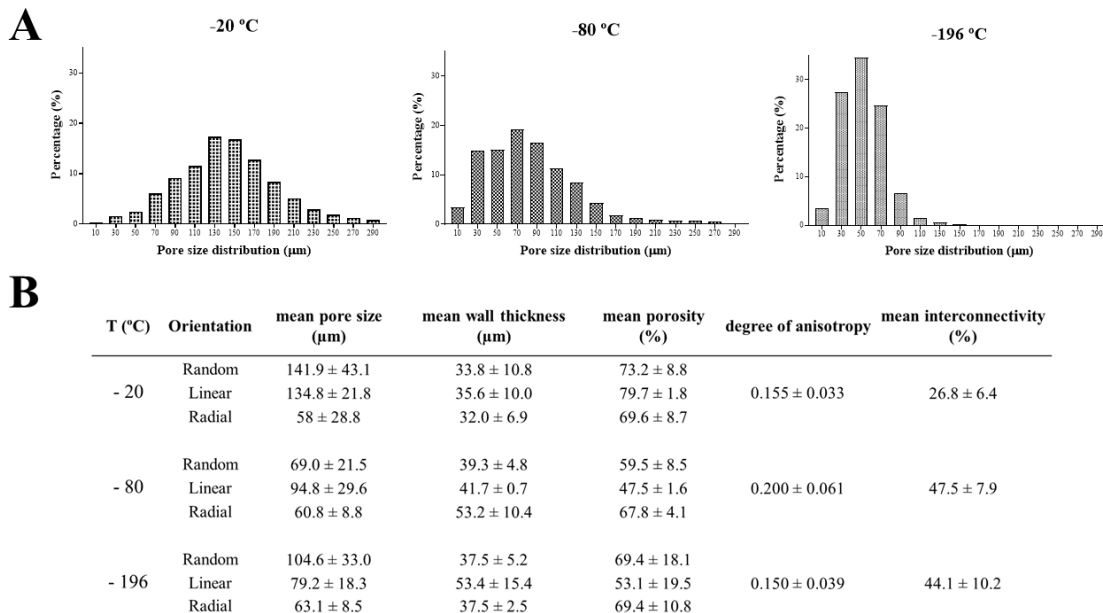
224
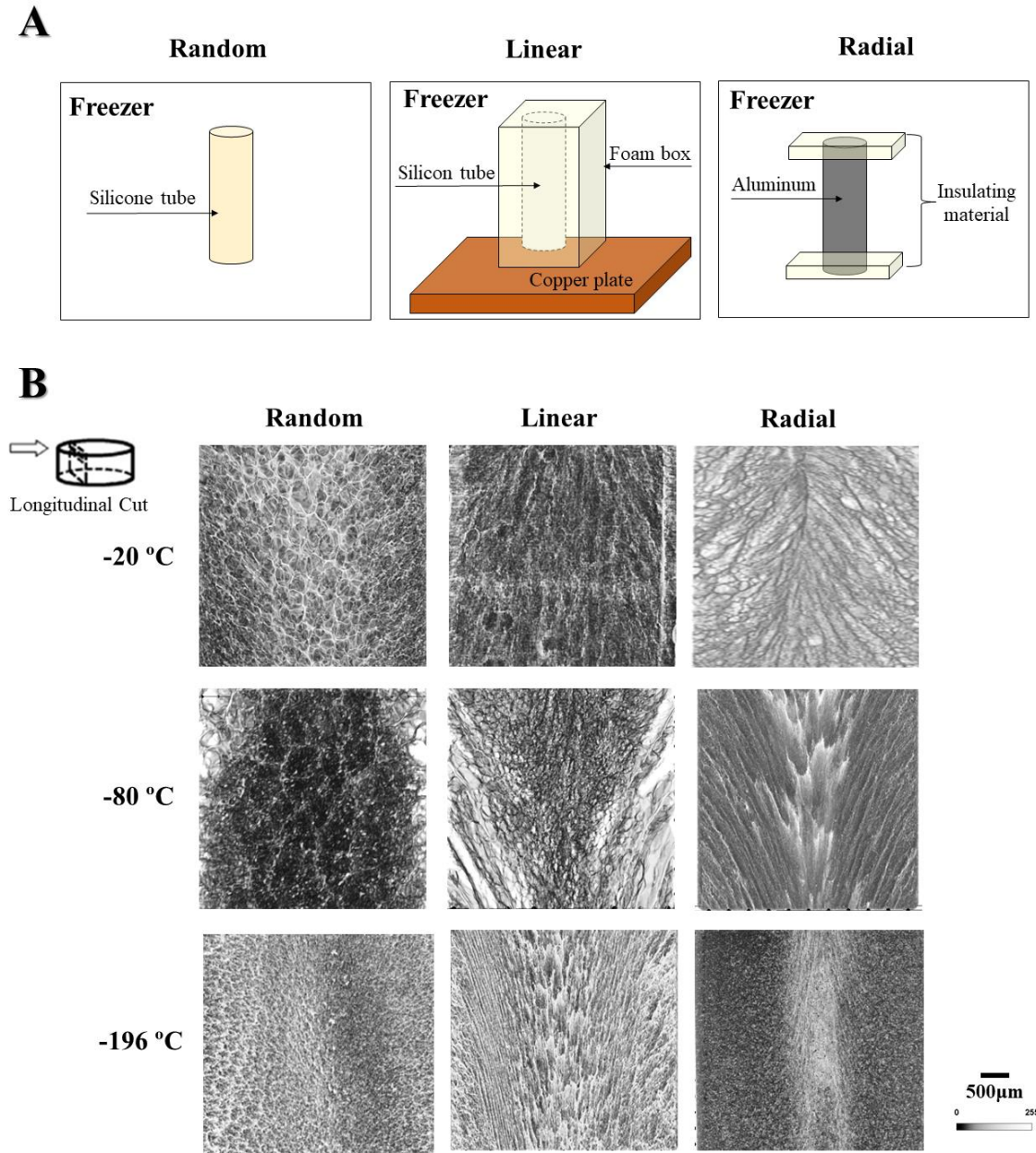
225

Figure 1. Scaffolds architecture controlled by ice-templating. A - Schematic representation of isotropic (random porosity) and anisotropic (linear and radial porosity) ice-templating process. **B -** Micro-CT 3D reconstruction of longitudinal views of random, linear, and radial oriented porosity of the ZnSr.TCP-SF scaffolds produced at -20 ºC, -80 ºC and -196 ºC (scale bar: 500 μm).

230

231 The morphometric quantitative analysis of the structures was evaluated using micro-CT

232 technique. For that, the pore size, pore distribution, pore wall thickness, porosity amount, degree

of anisotropy, and interconnectivity were assessed (Figure 2 B). The mean pore size was higher than 50 µm in every condition presenting a maximum of 141.9 µm for the random porosity achieved at -20 ℃. Accordingly, when using -20 ℃ during the freezing step, the average pore size was increased. In the summary of the 3D analysis, scaffolds presenting macropores larger than 300 µm and micropores that reached 5 µm were observed (data not shown). Regarding the dependency of mean pore size with pore directionality, linear and random orientations presented higher pore sizes. At -20 ℃ the mean pore size was 141.9 ± 43.1 µm followed by -80 ℃ (94.8 ± 29.6 µm) with the highest degree of anisotropy. Following, the mean wall thickness varies between 32.0 ± 6.9 and 53.4 ± 15.4 µm. The pores were distributed with a normal curve, also showing higher percentage of bigger pores for the scaffolds produced at -20℃ (Figure 2 A). It was noticed that the mean pore wall thickness tended to increase on both -196 ℃ and -80 ℃, which corroborates the visual observation of dense resulting structures when using lower temperatures due to a fast freezing and consequently, the creation of smaller ice crystals.

Generally, the mean porosity was kept between $47.5 \pm 1.6\%$ and $79.7 \pm 1.8\%$ for all the temperatures and orientations tested. However, this parameter decreased with the temperature. Finally, the lowest temperatures (-80 ℃ and -196 ℃) reinforced the pore alignment, as demonstrated by the higher degree of anisotropy. The highest interconnectivity was achieved at -80 ℃ ($47.5 \pm 7.9\%$), followed by -196 ℃ ($44.1 \pm 10.2\%$) and -20 ℃ ($26.8 \pm 6.4\%$). Thus, there was no linear tendency between interconnectivity and freezing temperature.

| T (℃)	Orientation	mean pore size (µm)	mean wall thickness (µm)	mean porosity (%)	degree of anisotropy	mean interconnectivity (%)
	Random	141.9 ± 43.1	33.8 ± 10.8	73.2 ± 8.8		
- 20	Linear	134.8 ± 21.8	35.6 ± 10.0	79.7 ± 1.8	0.155 ± 0.033	26.8 ± 6.4
	Radial	58 ± 28.8	32.0 ± 6.9	69.6 ± 8.7		
	Random	69.0 ± 21.5	39.3 ± 4.8	59.5 ± 8.5		
- 80	Linear	94.8 ± 29.6	41.7 ± 0.7	47.5 ± 1.6	0.200 ± 0.061	47.5 ± 7.9
	Radial	60.8 ± 8.8	53.2 ± 10.4	67.8 ± 4.1		
	Random	104.6 ± 33.0	37.5 ± 5.2	69.4 ± 18.1		
- 196	Linear	79.2 ± 18.3	53.4 ± 15.4	53.1 ± 19.5	0.150 ± 0.039	44.1 ± 10.2
	Radial	63.1 ± 8.5	37.5 ± 2.5	69.4 ± 10.8		

Figure 2. Physical characterization of the ice-templated ZnSr.TCP-SF scaffolds. A – Percentage of pore size distribution plot at -20, -80 and 196 ℃. **B -** Microstructure analysis at different temperatures with random, linear and radial pores obtained using the microCT technique (n= 3). Data shown as median ± Interquartile range.

258

259 The rheological analysis showed that frequency sweep oscillatory experiments were conducted in

260 a linear-viscoelastic regime (LVE) with the rehydrated scaffolds (Figure 3), obtained from

261 different condition combinations (random, linear, and radial at -196 ºC, -80 ºC and -20 ºC), at 37

262 ºC with a shear strain of 0.1%. An amplitude sweep test was beforehand performed to obtain the

263 Linear Viscoelastic Region, at 1 Hz of frequency and 37 ºC. A broad range of shear strain values

264 (ranging from 0.001% to 0.1%) with constant G' was obtained, showing well-dispersed and stable

265 systems.

266 The mechanical spectra shown on Figure 3, also known as frequency sweep tests, were obtained

267 by plotting the acquired values of storage and loss moduli (G'/Pa and G''/Pa, respectively) as

268 function of frequency (f/Hz). The initial instability of the values, and correspondent low

269 reliability, are characteristic regions of low frequencies and correspondent low sensibility of the

270 equipment, being inconclusive. Globally, the gel region was observed until 25 Hz, with a G'

271 plateau and after it, at high frequencies, the glassy behaviour was observed.[37]

272
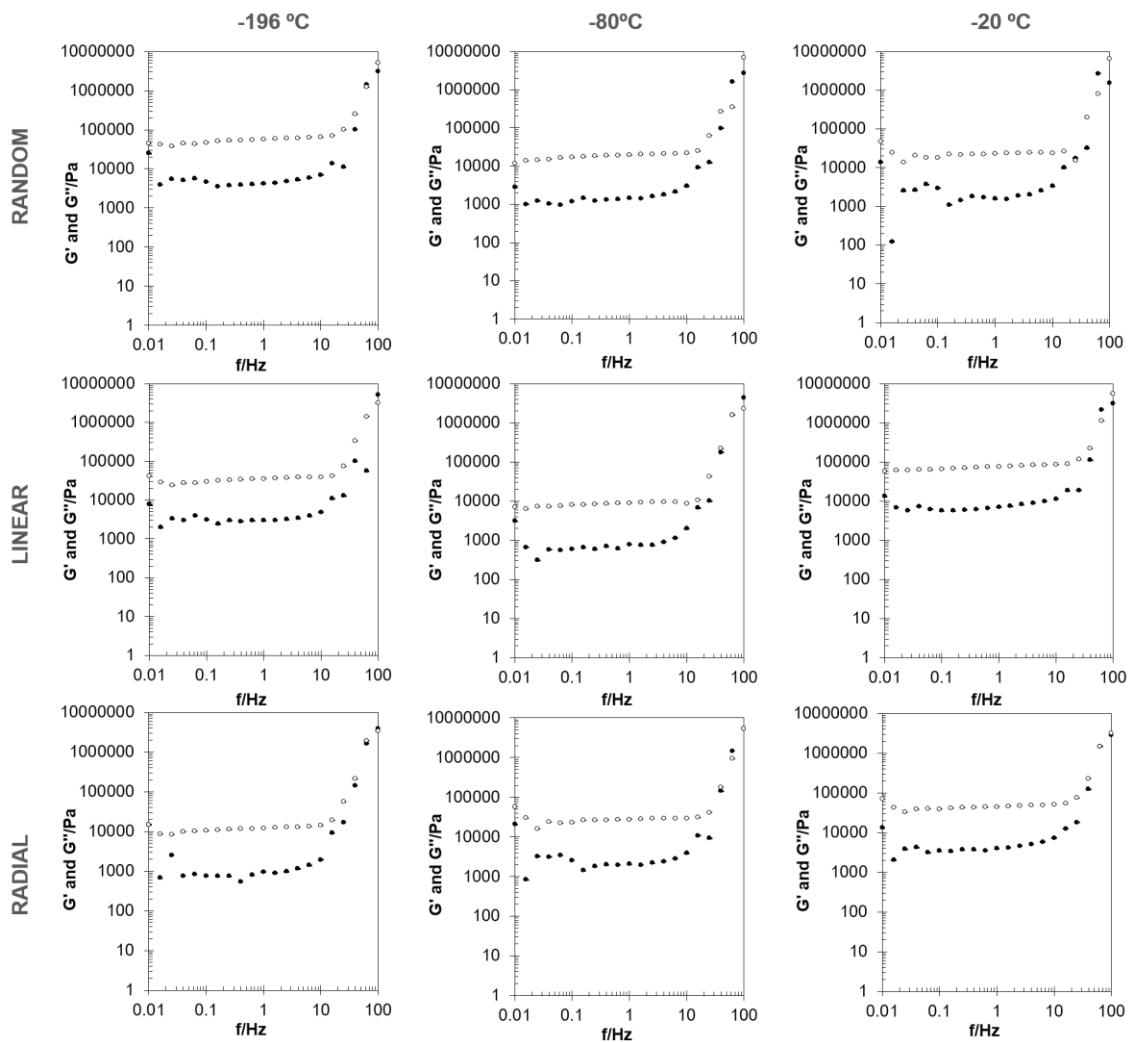
273

274 **Figure 3. Mechanical properties correlated with scaffolds' architectures.** Frequency sweeps for
275 random, linear and radial porous ZnSr.TCP-SF scaffolds produced at -196 ℃, -80 ℃ and -20 ℃. The
276 storage (*G'*/Pa) and loss (*G''*/Pa) moduli are represented by open symbol (○) and filled symbol (●),
277 respectively.

278

279 The plot presented in Figure 4 illustrates the effect of two fabrication parameters (temperature
280 and pore orientation) over the mechanical behavior (in terms of storage modulus, G'/Pa) of the
281 final product. Samples with higher storage modulus showed an increased solid character, which
282 suggested a greater strength or mechanical rigidity. Thus, the mechanical characteristics were
283 favored by the random orientation of the pores and temperature of -20 ℃. In contrast, the lower
284 storage modulus was achieved by the linear oriented scaffolds fabricated at -80 ℃.

285
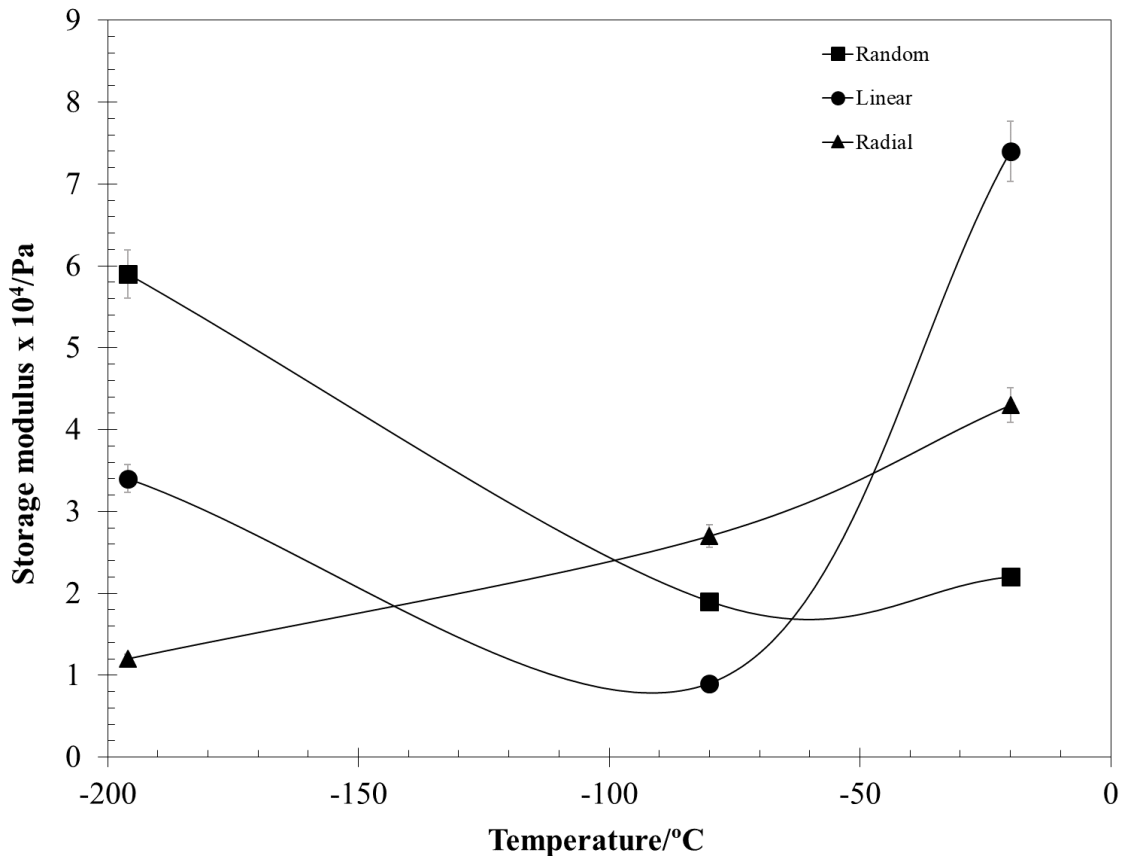
286

287 **Figure 4. Comparison between mechanical properties, pore orientation and applied freezing**
288 **temperature for the production of the ZnSr.TCP-SF scaffolds .** Surface chart plot of the average values
289 of storage modulus (G') obtained for the random, linear and radial porous ZnSr.TCP-SF scaffolds produced
290 at -196 ℃, -80 ℃, and -20 ℃.

291

Moreover, the samples prepared (i) at -80 °C with a linear pore orientation showed higher solid character, having a phase angle of (4.58 ± 0.05 °); (ii) at -80 °C with a random pore orientation (4.63 ± 0.04 °); and (iii) at -196 °C with a radial pore orientation (4.59 ± 0.05 °), with no statistically significant difference. Instead, the samples prepared with a random pore size at -196 °C had an average phase angle of (7.1 ± 0.2°), being the highest phase angle obtained, resulting in the scaffold of lowest solid character.

However, all samples had very low values of phase angle in the same order of magnitude, being in general very rigid scaffolds with the elastic modulus higher than the viscous modulus, throughout the tested frequencies.
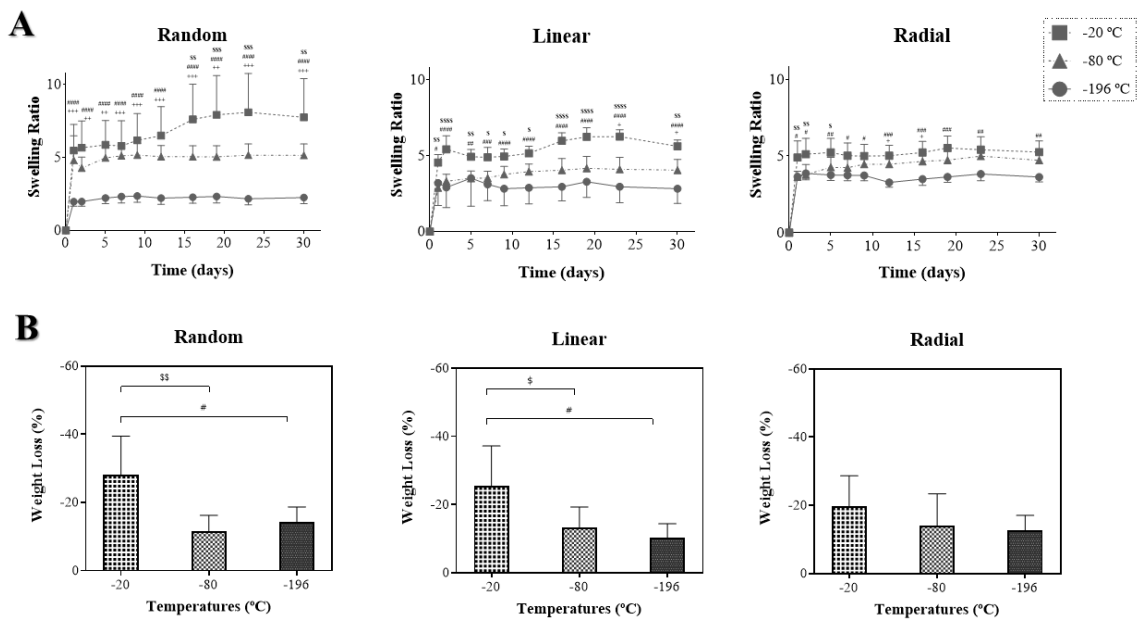
Figure 5. Swelling and weight loss dynamics of the fabricated scaffolds. A- Swelling ratio of the ZnSr.TCP-SF scaffolds with random, linear and radial orientation produced at -20 °C, -80 °C and -196 °C by hydration in PBS over 30 days. Statistical differences between temperatures (°C) are represented by: (**$**) for -20 | -80; (**#**) for -20 | -196 and (**+**) for -80 | -196. **B**- Percentage of weight loss of the ZnSr.TCP-SF scaffolds produced having radial, linear and random pore orientation and produced at -20 °C, -80°C and -196 °C, after 30 days in PBS and drying overnight at 37 °C. Data shown as mean ± standard deviation (SD). Statistical differences for swelling were determined using Two-Way ANOVA and for weight loss One-Way ANOVA with Tukey's multiple comparisons test (N = 6). *p<0.05, ** p<0.01 *** p<0.001, **** p<0.0001.

Regarding the swelling ration (SR) and weight loss were carried out to predict the stability of the structures (Figure 5). Results showed a small increase of the SR of the structures after immersion in PBS at 37 °C for the 30 d (SR between 5 - 15 %), with statistical difference in each pore orientation specially between the freezing temperatures: -20 °C and -196 °C (Figure 5A). These

data denote the capacity of the scaffolds to accommodate water inside their porous network, thereby increasing their volume over time. The SR results demonstrate that all the samples are in equilibrium between days 5 and 15. At this point there is an increase in the SR, which was more denoted for random and linear pore orientation. The SR shows correlation with the freezing temperature. A higher SR for the scaffolds frozen at -20 ℃ was observed, whereas the lowest SR was obtained for the scaffolds produced at -196 ℃ (smaller pore size), behavior maintained in all three pore orientations.

Regarding the weight loss (Figure 5B), the structures presented a tendency of mass loss of ~15 - 20 % for scaffolds with smaller pores, i.e. produced at -196 ℃ and ~20 - 40% for the scaffolds produced at -20 ℃ for all the pores orientations. This means that at -196 ℃, a lower degradation was observed, which is in accordance with the pore size, implying minor fluid uptake in the scaffolds with smaller pore size. Consequently, at the highest applied freezing temperature (-20 ℃), the hydration mechanism was improved due to the larger mean pore size, resulting in a higher weight loss. The data presented significant differences between -20 ℃ and -80 ℃, as well as, -20 ℃ and 196 ℃ in random and linear porous structures. However, in radial pore orientation the behavior is very homogeneous, independently of the temperature of freezing.

4. Discussion

When designing scaffolds, the main pre-requisite to attain is to obtain structures having proper porosity with suitable diameter, that mimic the native tissue ECM, and allow the distribution of nutrients and the removal of waste products.[38] For that, several studies have emerged showing conflicting data regarding the most suitable pore size for bone TE application. The first studies established that the optimal required pore size show to be 100–135 µm.[39,40] However, later reports indicated pores > 300 µm to allow bone ingrowth and vascularization.[41–43] Still, smaller pores also allow the ossification of osteochondral tissue.[44,45] Besides, fibrocartilaginous tissue need 200-300 µm to properly growth.[46]

To achieve the optimal pores size requirements several techniques (magnetic assembly,[47] photolithography,[48] bioprinting,[49] electrospinning[50]) have been shown 3D scaffolds fabrication with controlled networks, but mechanical properties limited biological applications, which, along with high costs and complex fabrication methodologies, present major difficulties to their clinical translation.[51] For that reason, in this work we applied the ice-templating processing which is an easy and fast technique that enables to design advanced scaffolds with uniform and highly interconnected porous structures. In this sense, freezing conditions can be altered to obtain the most suitable pore size and shape, allowing a proper regeneration process.[52] Herein, it was demonstrated a decrease of pore size with the decrease of the freezing temperature (Figure 2), which is in close agreement with a study by Xu *et al.*[53] where it was observed that the pore size

353 was tightly associated with the freezing temperatures in scaffold fabricated by freeze-drying,

354 decreasing as temperature decreases. Likewise, as previously published by our group, the

355 scaffolds produced at -196 °C experienced the fastest freezing in which ice crystals had no time

356 to grow in width, producing a more compact structure and generally a lower mean pore size.[54]

357 Similarly, Zhang et al,[55] also showed that linear pore alignment is efficiently formed due to the

358 faster growth kinetics of ice crystals vertical growth, thus creating thicker walls than when using

359 radial freezing. The scaffolds are described with a pore size ranging from 25 to 120 μm, being

360 produced between −60 °C and −75 °C freezing temperatures, similarly to what we have observed.

361 However, here we apply ice-templating in combination of biomaterials, the ZnSr.TCP-SF

362 composite, with programmable pore alignments, including the radial orientation, which are for

363 example interesting for cortical bone defects and modulation.[5,6] The use of SF represents an

364 potential additional advantage due to its slow degradation, which is beneficial to improve bone

365 regeneration. Normally, bone loss takes over 6 to 12 months of healing so the use of engineered

366 scaffolds to support tissue regeneration should address the required natural tissue regeneration

367 time.[56,57]

368 The obtained results from the present work give an insight of the structural and mechanical

369 characteristics of the fabricated scaffolds. Changes in pore size and orientation influence the

370 mechanical/elastic properties of the scaffolds.[58] Correspondingly, the rheological study showed

371 that, in general, all samples behaved like strong solids, with the elastic modulus higher than the

372 viscous one throughout the frequency sweep. On the contrary, previous studies using only SF

373 crosslinked by the enzymatic complex HRP/H_2O_2 showed viscoelastic solid behaviour.[59]

374 Therefore, the increased solid performance in ZnSr.TCP-SF scaffolds was reinforced by the

375 presence of TCP in the SF scaffolds, which also disguises the brittleness associated to TCP.[60,61]

376 Additionally, the storage modulus provided an indication about the sample aptitude to store

377 deformation energy in an elastic manner. The maximum G' plateau was achieved by the samples

378 with random and linear porous orientation at -196 °C. This observation could be explained by the

379 scaffolds high density when produced with this temperature, because the fast formation of ice

380 crystals when using very low freezing temperatures originates small mean pore size after

381 lyophilization and consequently more rigid structures.[53] Moreover, the samples showing lower

382 storage modulus were those prepared with linear orientation at -80 °C. In fact, globally the

383 samples prepared at -80 °C presented the lower elasticity.

384 The swelling capacity is an essential property of scaffolds as it influences the exchange of cell

385 nutrients, oxygen, and other metabolites. This hydration process increases pore diameter

386 improving the internal surface area of scaffolds, which may be relevant to support the fitting of

387 the implanted structure into a targeted injured tissue. Though, under physiological conditions, the

388 swelling needs to be controlled since it influences the degradation rate of the scaffolds.[62] In that

389 sense, SR results showed that as immersion time passed, the structures kept their integrity and

apparent morphology indicating their stability. Nevertheless, it were demonstrated significant differences between the temperatures of freezing in which the scaffolds were obtained (-20 ℃, -80 ℃ and -196 ℃) and their SR. Scaffolds produced at -20 ℃ had higher swelling and higher mass loss due to their higher pore size, facilitating hydration and consequently degradation. Therefore, structures manufactured using the other two temperatures (-80 ℃ and -196 ℃) present themselves as more viable to achieve a long-lasting implantation into osteochondral tissue. This fact reinforces again the possibility of using our aligned used scaffolds in bone regeneration with the certainty of providing proper support for new tissue.

The protein adsorption was also assessed (data not shown) because it denotes the first process that occurs after the scaffold implantation. This process changes the properties of the surface activating the immune system and inducing regeneration.[63,64] Unwanted protein adsorption may prevent cell-biomaterial interactions, so this process is strongly influenced by the composition of the surface of the biomaterial. The data disclosed in the present work indicate that the produced scaffolds adsorbed around 1.5 mg/mL of BSA in solution independently of the pore size, which represents about 43 % (w/w) of the stock solution. It is important to have into consideration that scaffolds containing TCP were previously reported to promote absorption of serum protein resulting in cell adhesion and collagen secretion.[65] However, the impact of the produced scaffolds on protein adsorption also happens due to the presence of SF, since it was previously proven that SF induces protein adsorption either by hydrophobic and electrostatic interactions or covalent binding to the β-chain.[66]

Although it was demonstrated herein that by means of using low fabrication temperatures and ice-templating it is possible to produce porous SF-based scaffolds with guided morphology, further studies should aim at increasing the pore size of ZnSr.TCP-SF scaffolds. A general consensus regarding the pore size for proper osteogenesis and vascularization, indicates that pores should have superior to 300 μm.[41–43] In this sense, changing the chemical composition of the scaffolds could be a possible way to tune this parameter namely with the decrease of SF concentration.[67] Finally, studies with stem cells should be carried out to understand the impact of pore orientation and size on cell differentiation, as well as to assess the ability of cell invasion into the different scaffolds.

5. Conclusions

ZnSr.TCP-SF scaffolds were fabricated with high-porosity and interconnected pores, using ice-templating with linear, radial, and random architectures for bone TE and regenerative medicine purposes. The produced scaffolds' pore size, shape and orientation was directly controlled by the fabrication set-up, using insulation and thermally-conductive freezing molds. At the lowest freezing temperature (-196 ℃), a higher pore alignment was obtained, while applying -20 ℃ the

427 pore diameter of the structures was increased. Rheological studies pointed out a solid behavior
428 reinforced by ionic-doped TCP incorporation, which represents an increased advantage for bone
429 TE applications. Overall, a scalable and cost-effective method is presented to tailor pore
430 orientation, size, and shape into SF structures with potential to be applied for the regeneration of
431 anisotropic hard tissues.

432

440

441 **References**

442 (1)   Caliari, S. R.; Harley, B. A. C. The Effect of Anisotropic Collagen-GAG Scaffolds and Growth Factor
443   Supplementation on Tendon Cell Recruitment, Alignment, and Metabolic Activity. *Biomaterials* **2011**, *32*
444   (23), 5330–5340. https://doi.org/10.1016/j.biomaterials.2011.04.021.

445 (2)   Damania, D.; Subramanian, H.; Tiwari, A. K.; Stypula, Y.; Kunte, D.; Pradhan, P.; Roy, H. K.; Backman, V.
446   Role of Cytoskeleton in Controlling the Disorder Strength of Cellular Nanoscale Architecture. *Biophys. J.*
447   **2010**. https://doi.org/10.1016/j.bpj.2010.05.023.

448 (3)   Zhang, H.; Hussain, I.; Brust, M.; Butler, M. F.; Rannard, S. P.; Cooper, A. I. Aligned Two- and Three-
449   Dimensional Structures by Directional Freezing of Polymers and Nanoparticles. *Nat. Mater.* **2005**, *4* (10),
450   787–793. https://doi.org/10.1038/nmat1487.

451 (4)   Davenport, R. J. What Controls Organ Regeneration. *Science*. American Association for the Advancement of
452   Science July 1, 2005, p 84. https://doi.org/10.1126/science.309.5731.84.

453 (5)   Di Luca, A.; Longoni, A.; Criscenti, G.; Mota, C.; Van Blitterswijk, C.; Moroni, L. Toward Mimicking the
454   Bone Structure: Design of Novel Hierarchical Scaffolds with a Tailored Radial Porosity Gradient.
455   *Biofabrication* **2016**. https://doi.org/10.1088/1758-5090/8/4/045007.

456 (6)   Gordon, K. D.; Duck, T. R.; King, G. J. W.; Johnson, J. A. Mechanical Properties of Subchondral Cancellous
457   Bone of the Radial Head. *J. Orthop. Trauma* **2003**, *17* (4), 285–289. https://doi.org/10.1097/00005131-
458   200304000-00007.

459 (7)   Rho, J. Y.; Kuhn-Spearing, L.; Zioupos, P. Mechanical Properties and the Hierarchical Structure of Bone.
460   *Med. Eng. Phys.* **1998**. https://doi.org/10.1016/S1350-4533(98)00007-1.

461 (8)   Clarke, B. Normal Bone Anatomy and Physiology. *Clinical journal of the American Society of Nephrology :*
462   *CJASN*. 2008. https://doi.org/10.2215/CJN.04151206.

463 (9)   Wahl, D. A.; Czernuszka, J. T. Collagen-Hydroxyapatite Composites for Hard Tissue Repair. *European Cells*

464   *and Materials*. 2006, pp 43–56. https://doi.org/10.22203/eCM.v011a06.

465   (10) Zhang, D.; Wu, X.; Chen, J.; Lin, K. The Development of Collagen Based Composite Scaffolds for Bone
466   Regeneration. *Bioactive Materials*. 2018. https://doi.org/10.1016/j.bioactmat.2017.08.004.

467   (11) Sai, Y.; Shiwaku, Y.; Anada, T.; Tsuchiya, K.; Takahashi, T.; Suzuki, O. Capacity of Octacalcium Phosphate
468   to Promote Osteoblastic Differentiation toward Osteocytes in Vitro. *Acta Biomater.* **2018**.
469   https://doi.org/10.1016/j.actbio.2018.01.026.

470   (12) O'Hare, P.; Meenan, B. J.; Burke, G. A.; Byrne, G.; Dowling, D.; Hunt, J. A. Biological Responses to
471   Hydroxyapatite Surfaces Deposited via a Co-Incident Microblasting Technique. *Biomaterials* **2010**.
472   https://doi.org/10.1016/j.biomaterials.2009.09.067.

473   (13) Bose, S.; Fielding, G.; Tarafder, S.; Bandyopadhyay, A. Understanding of Dopant-Induced Osteogenesis and
474   Angiogenesis in Calcium Phosphate Ceramics. *Trends Biotechnol.* **2013**, *31* (10), 594–605.
475   https://doi.org/10.1016/j.tibtech.2013.06.005.

476   (14) Roy, M.; Fielding, G. A.; Bandyopadhyay, A.; Bose, S. Effects of Zinc and Strontium Substitution in
477   Tricalcium Phosphate on Osteoclast Differentiation and Resorption. *Biomater. Sci.* **2013**, *1* (1), 74–82.
478   https://doi.org/10.1039/C2BM00012A.

479   (15) Pina, S.; Oliveira, J. M.; Reis, R. L. Natural-Based Nanocomposites for Bone Tissue Engineering and
480   Regenerative Medicine: A Review. *Adv. Mater.* **2015**, *27* (7), 1143–1169.
481   https://doi.org/10.1002/adma.201403354.

482   (16) Ribeiro, V. P.; Pina, S.; Costa, J. B.; Cengiz, I. F.; García-Fernández, L.; Fernández-Gutiérrez, M. D. M.;
483   Paiva, O. C.; Oliveira, A. L.; San-Román, J.; Oliveira, J. M.; Reis, R. L. Enzymatically Cross-Linked Silk
484   Fibroin-Based Hierarchical Scaffolds for Osteochondral Regeneration. *ACS Appl. Mater. Interfaces* **2019**, *11*
485   (4), 3781–3799. https://doi.org/10.1021/acsami.8b21259.

486   (17) Pina, S.; Canadas, R. F.; Jiménez, G.; Perán, M.; Marchal, J. A.; Reis, R. L.; Oliveira, J. M. Biofunctional
487   Ionic-Doped Calcium Phosphates: Silk Fibroin Composites for Bone Tissue Engineering Scaffolding. *Cells
488   Tissues Organs* **2017**, *204* (3–4), 150–163. https://doi.org/10.1159/000469703.

489   (18) V.P. Ribeiro, S. Pina, R.F. Canadas, A.S. Morais, C. Vilela, S. Vieira, I. Cengiz, R. Reis, J. M. O. In Vivo
490   Performance of Hierarchical HRP-Crosslinked Silk Fibroin/β-TCP Scaffolds for Osteochondral Tissue
491   Regeneration. *Regen. Med. Front.* **2019**. https://doi.org/10.20900/rmf20190007.

492   (19) Rockwood, D. N.; Preda, R. C.; Yücel, T.; Wang, X.; Lovett, M. L.; Kaplan, D. L. Materials Fabrication from
493   Bombyx Mori Silk Fibroin. *Nat. Protoc.* **2011**, *6* (10), 1612–1631. https://doi.org/10.1038/nprot.2011.379.

494   (20) Vepari, C.; Kaplan, D. L. Silk as a Biomaterial. *Progress in Polymer Science (Oxford)*. 2007.
495   https://doi.org/10.1016/j.progpolymsci.2007.05.013.

496   (21) Hofmann, S.; Hilbe, M.; Fajardo, R. J.; Hagenmüller, H.; Nuss, K.; Arras, M.; Müller, R.; Von Rechenberg,
497   B.; Kaplan, D. L.; Merkle, H. P.; Meinel, L. Remodeling of Tissue-Engineered Bone Structures in Vivo. *Eur.
498   J. Pharm. Biopharm.* **2013**, *85* (1), 119–129. https://doi.org/10.1016/j.ejpb.2013.02.011.

499   (22) Partlow, B. P.; Hanna, C. W.; Rnjak-Kovacina, J.; Moreau, J. E.; Applegate, M. B.; Burke, K. A.; Marelli, B.;
500   Mitropoulos, A. N.; Omenetto, F. G.; Kaplan, D. L. Highly Tunable Elastomeric Silk Biomaterials. *Adv. Funct.
501   Mater.* **2014**, *24* (29), 4615–4624. https://doi.org/10.1002/adfm.201400526.

502   (23)   Ribeiro, V. P.; da Silva Morais, A.; Maia, F. R.; Canadas, R. F.; Costa, J. B.; Oliveira, A. L.; Oliveira, J. M.;
503   Reis, R. L. Combinatory Approach for Developing Silk Fibroin Scaffolds for Cartilage Regeneration. *Acta*
504   *Biomater.* **2018**. https://doi.org/10.1016/j.actbio.2018.03.047.

505   (24)   Marelli, B.; Ghezzi, C. E.; Alessandrino, A.; Barralet, J. E.; Freddi, G.; Nazhat, S. N. Silk Fibroin Derived
506   Polypeptide-Induced Biomineralization of Collagen. *Biomaterials* **2012**, *33* (1), 102–108.
507   https://doi.org/10.1016/J.BIOMATERIALS.2011.09.039.

508   (25)   Gao, C.; Peng, S.; Feng, P.; Shuai, C. Bone Biomaterials and Interactions with Stem Cells. *Bone Research.*
509   2017. https://doi.org/10.1038/boneres.2017.59.

510   (26)   Gutiérrez, M. C.; Ferrer, M. L.; del Monte, F. Ice-Templated Materials: Sophisticated Structures Exhibiting
511   Enhanced Functionalities Obtained after Unidirectional Freezing and Ice-Segregation-Induced Self-Assembly
512   †. *Chem. Mater.* **2008**, *20* (3), 634–648. https://doi.org/10.1021/cm702028z.

513   (27)   Annabi, N.; Nichol, J. W.; Zhong, X.; Ji, C.; Koshy, S.; Khademhosseini, A.; Dehghani, F. Controlling the
514   Porosity and Microarchitecture of Hydrogels for Tissue Engineering. *Tissue Eng. Part B Rev.* **2010**, *16* (4),
515   371–383. https://doi.org/10.1089/ten.teb.2009.0639.

516   (28)   Petersen, A.; Princ, A.; Korus, G.; Ellinghaus, A.; Leemhuis, H.; Herrera, A.; Klaumünzer, A.; Schreivogel,
517   S.; Woloszyk, A.; Schmidt-Bleek, K.; Geissler, S.; Heschel, I.; Duda, G. N. A Biomaterial with a Channel-
518   like Pore Architecture Induces Endochondral Healing of Bone Defects. *Nat. Commun.* **2018**, *9* (1), 1–16.
519   https://doi.org/10.1038/s41467-018-06504-7.

520   (29)   Yan, L.-P.; Oliveira, J. M.; Oliveira, A. L.; Caridade, S. G.; Mano, J. F.; Reis, R. L. Macro/Microporous Silk
521   Fibroin Scaffolds with Potential for Articular Cartilage and Meniscus Tissue Engineering Applications. *Acta*
522   *Biomater.* **2012**, *8* (1), 289–301. https://doi.org/10.1016/J.ACTBIO.2011.09.037.

523   (30)   Pina, S.; Vieira, S.; Rego, P.; Torres, P.; da Cruz e Silva, O.; da Cruz e Silva, E.; Ferreira, J. Biological
524   Responses of Brushite-Forming Zn- and ZnSr- Substituted Beta-Tricalcium Phosphate Bone Cements. *Eur.*
525   *Cells Mater.* **2010**, *20*, 162–177. https://doi.org/10.22203/ecm.v020a14.

526   (31)   Canadas, R. F.; Ren, T.; Tocchio, A.; Marques, A. P.; Oliveira, J. M.; Reis, R. L.; Demirci, U. Tunable
527   Anisotropic Networks for 3-D Oriented Neural Tissue Models. *Biomaterials* **2018**.
528   https://doi.org/10.1016/j.biomaterials.2018.07.055.

529   (32)   Canadas, R. F.; Ren, T.; Marques, A. P.; Oliveira, J. M.; Reis, R. L.; Demirci, U. Biochemical Gradients to
530   Generate 3D Heterotypic-Like Tissues with Isotropic and Anisotropic Architectures. *Adv. Funct. Mater.* **2018**,
531   *28* (48), 1804148. https://doi.org/10.1002/adfm.201804148.

532   (33)   Harley, B. A.; Hastings, A. Z.; Yannas, I. V.; Sannino, A. Fabricating Tubular Scaffolds with a Radial Pore
533   Size Gradient by a Spinning Technique. *Biomaterials* **2006**, *27* (6), 866–874.
534   https://doi.org/10.1016/j.biomaterials.2005.07.012.

535   (34)   Shin, Y. M.; Shin, H. J.; Yang, D. H.; Koh, Y. J.; Shin, H.; Chun, H. J. Advanced Capability of Radially
536   Aligned Fibrous Scaffolds Coated with Polydopamine for Guiding Directional Migration of Human
537   Mesenchymal Stem Cells. *J. Mater. Chem. B* **2017**, *5* (44), 8725–8737. https://doi.org/10.1039/c7tb01758h.

538   (35)   Scotti, K. L.; Dunand, D. C. Freeze Casting – A Review of Processing, Microstructure and Properties via the
539   Open Data Repository, FreezeCasting.Net. *Progress in Materials Science.* 2018, pp 243–305.
540   https://doi.org/10.1016/j.pmatsci.2018.01.001.

541   (36)   Tabilo-Munizaga, G.; Barbosa-Cánovas, G. V. Rheology for the Food Industry. *J. Food Eng.* **2005**.
542   https://doi.org/10.1016/j.jfoodeng.2004.05.062.

543   (37)   Zuidema, J. M.; Rivet, C. J.; Gilbert, R. J.; Morrison, F. A. A Protocol for Rheological Characterization of
544   Hydrogels for Tissue Engineering Strategies. *J. Biomed. Mater. Res. Part B Appl. Biomater.* **2014**, *102* (5),
545   1063–1073. https://doi.org/10.1002/jbm.b.33088.

546   (38)   Murphy, C. M.; O'Brien, F. J. Understanding the Effect of Mean Pore Size on Cell Activity in Collagen-
547   Glycosaminoglycan Scaffolds. *Cell Adhesion and Migration*. Taylor and Francis Inc. 2010, pp 377–381.
548   https://doi.org/10.4161/cam.4.3.11747.

549   (39)   Hulbert, S. F.; Young, F. A.; Mathews, R. S.; Klawitter, J. J.; Talbert, C. D.; Stelling, F. H. Potential of
550   Ceramic Materials as Permanently Implantable Skeletal Prostheses. *J. Biomed. Mater. Res.* **1970**, *4* (3), 433–
551   456. https://doi.org/10.1002/jbm.820040309.

552   (40)   Klawitter, J. J.; Bagwell, J. G.; Weinstein, A. M.; Sauer, B. W.; Pruitt, J. R. An Evaluation of Bone Growth
553   into Porous High Density Polyethylene. *J. Biomed. Mater. Res.* **1976**, *10* (2), 311–323.
554   https://doi.org/10.1002/jbm.820100212.

555   (41)   Jones, A. C.; Arns, C. H.; Sheppard, A. P.; Hutmacher, D. W.; Milthorpe, B. K.; Knackstedt, M. A. Assessment
556   of Bone Ingrowth into Porous Biomaterials Using MICRO-CT. *Biomaterials* **2007**, *28* (15), 2491–2504.
557   https://doi.org/10.1016/j.biomaterials.2007.01.046.

558   (42)   Karageorgiou, V.; Kaplan, D. Porosity of 3D Biomaterial Scaffolds and Osteogenesis. *Biomaterials*. 2005, pp
559   5474–5491. https://doi.org/10.1016/j.biomaterials.2005.02.002.

560   (43)   Nazarov, R.; Jin, H. J.; Kaplan, D. L. Porous 3-D Scaffolds from Regenerated Silk Fibroin.
561   *Biomacromolecules* **2004**. https://doi.org/10.1021/bm034327e.

562   (44)   Tsuruga, E.; Takita, H.; Itoh, H.; Wakisaka, Y.; Kuboki, Y. Pore Size of Porous Hydroxyapatite as the Cell-
563   Substratum Controls BMP-Induced Osteogenesis. *J. Biochem.* **1997**, *121* (2), 317–324.
564   https://doi.org/10.1093/oxfordjournals.jbchem.a021589.

565   (45)   Mantila Roosa, S. M.; Kemppainen, J. M.; Moffitt, E. N.; Krebsbach, P. H.; Hollister, S. J. The Pore Size of
566   Polycaprolactone Scaffolds Has Limited Influence on Bone Regeneration in an in Vivo Model. *J. Biomed.*
567   *Mater. Res. - Part A* **2010**, *92* (1), 359–368. https://doi.org/10.1002/jbm.a.32381.

568   (46)   Elema, H.; de Groot, J. H.; Nijenhuis, A. J.; Pennings, A. J.; Veth, R. P. H.; Klompmaker, J.; Jansen, H. W.
569   B. Use of Porous Biodegradable Polymer Implants in Meniscus Reconstruction. 2) Biological Evaluation of
570   Porous Biodegradable Polymer Implants in Menisci. *Colloid Polym. Sci.* **1990**, *268* (12), 1082–1088.
571   https://doi.org/10.1007/BF01410673.

572   (47)   Xu, F.; Wu, C. A. M.; Rengarajan, V.; Finley, T. D.; Keles, H. O.; Sung, Y.; Li, B.; Gurkan, U. A.; Demirci,
573   U. Three-Dimensional Magnetic Assembly of Microscale Hydrogels. *Adv. Mater.* **2011**.
574   https://doi.org/10.1002/adma.201101962.

575   (48)   Gurkan, U. A.; Fan, Y.; Xu, F.; Erkmen, B.; Urkac, E. S.; Parlakgul, G.; Bernstein, J.; Xing, W.; Boyden, E.
576   S.; Demirci, U. Simple Precision Creation of Digitally Specified, Spatially Heterogeneous, Engineered Tissue
577   Architectures. *Adv. Mater.* **2013**. https://doi.org/10.1002/adma.201203261.

578   (49)   Nyberg, E.; Rindone, A.; Dorafshar, A.; Grayson, W. L. Comparison of 3D-Printed Poly-ϵ-Caprolactone

Scaffolds Functionalized with Tricalcium Phosphate, Hydroxyapatite, Bio-Oss, or Decellularized Bone Matrix. *Tissue Eng. - Part A* **2017**. https://doi.org/10.1089/ten.tea.2016.0418.

(50) Jun, I.; Han, H. S.; Edwards, J. R.; Jeon, H. Electrospun Fibrous Scaffolds for Tissue Engineering: Viewpoints on Architecture and Fabrication. *International Journal of Molecular Sciences*. 2018. https://doi.org/10.3390/ijms19030745.

(51) Chocholata, P.; Kulda, V.; Babuska, V. Fabrication of Scaffolds for Bone-Tissue Regeneration. *Materials*. 2019. https://doi.org/10.3390/ma12040568.

(52) Zmora, S.; Glicklis, R.; Cohen, S. Tailoring the Pore Architecture in 3-D Alginate Scaffolds by Controlling the Freezing Regime during Fabrication. *Biomaterials* **2002**, *23* (20), 4087–4094. https://doi.org/10.1016/S0142-9612(02)00146-1.

(53) Xu, Y.; Zhang, D.; Wang, Z. L.; Gao, Z. T.; Zhang, P. B.; Chen, X. S. Preparation of Porous Nanocomposite Scaffolds with Honeycomb Monolith Structure by One Phase Solution Freezedrying Method. *Chinese J. Polym. Sci. (English Ed.* **2011**, *29* (2), 215–224. https://doi.org/10.1007/s10118-010-1015-5.

(54) Reys, L. L.; Silva, S. S.; Pirraco, R. P.; Marques, A. P.; Mano, J. F.; Silva, T. H.; Reis, R. L. Influence of Freezing Temperature and Deacetylation Degree on the Performance of Freeze-Dried Chitosan Scaffolds towards Cartilage Tissue Engineering. *Eur. Polym. J.* **2017**, *95*, 232–240. https://doi.org/10.1016/j.eurpolymj.2017.08.017.

(55) Zhang, Y.; Wang, C.; Jiang, W.; Zuo, W.; Han, G. Influence of Stage Cooling Method on Pore Architecture of Biomimetic Alginate Scaffolds. *Sci. Rep.* **2017**, *7* (1), 1–8. https://doi.org/10.1038/s41598-017-16024-x.

(56) L. Schropp, A. Wenzel, L. Kostopoulos, T. K. Bone Healing and Soft Tissue Contour Changes Following Single-Tooth Extraction: A Clinical and Radiographic 12-Month Prospective Study. *J. Prosthet. Dent.* **2004**. https://doi.org/10.1016/j.prosdent.2003.10.022.

(57) Liu, J.; Kerns, D. G. Mechanisms of Guided Bone Regeneration: A Review. *Open Dent. J.* **2014**. https://doi.org/10.2174/1874210601408010056.

(58) Fuller, K. P.; Gaspar, D.; Delgado, L. M.; Pandit, A.; Zeugolis, D. I. Influence of Porosity and Pore Shape on Structural, Mechanical and Biological Properties of Poly ε-Caprolactone Electro-Spun Fibrous Scaffolds. *Nanomedicine* **2016**, *11* (9), 1031–1040. https://doi.org/10.2217/nnm.16.21.

(59) Ribeiro, V. P.; Silva-Correia, J.; Gonçalves, C.; Pina, S.; Radhouani, H.; Montonen, T.; Hyttinen, J.; Roy, A.; Oliveira, A. L.; Reis, R. L.; Oliveira, J. M. Rapidly Responsive Silk Fibroin Hydrogels as an Artificial Matrix for the Programmed Tumor Cells Death. *PLoS One* **2018**, *13* (4). https://doi.org/10.1371/journal.pone.0194441.

(60) Kaully, T.; Siegmann, A.; Shacham, D. Rheology of Highly Filled Natural CaCO3 Composites. II. Effects of Solid Loading and Particle Size Distribution on Rotational Rheometry. *Polym. Compos.* **2007**, *28* (4), 524–533. https://doi.org/10.1002/pc.20309.

(61) Huang, B.; Bártolo, P. J. Rheological Characterization of Polymer/Ceramic Blends for 3D Printing of Bone Scaffolds. *Polym. Test.* **2018**, *68*, 365–378. https://doi.org/10.1016/j.polymertesting.2018.04.033.

(62) Maji, K.; Dasgupta, S.; Pramanik, K.; Bissoyi, A. Preparation and Evaluation of Gelatin-Chitosan-Nanobioglass 3D Porous Scaffold for Bone Tissue Engineering. *Int. J. Biomater.* **2016**, *2016*, 9825659.

617   https://doi.org/10.1155/2016/9825659.

618   (63)   Vogler, E. A. Protein Adsorption in Three Dimensions. *Biomaterials* **2012**.
619   https://doi.org/10.1016/j.biomaterials.2011.10.059.

620   (64)   Wei, Q.; Becherer, T.; Angioletti-Uberti, S.; Dzubiella, J.; Wischke, C.; Neffe, A. T.; Lendlein, A.; Ballauff,
621   M.; Haag, R. Protein Interactions with Polymer Coatings and Biomaterials. *Angewandte Chemie -*
622   *International Edition*. 2014. https://doi.org/10.1002/anie.201400546.

623   (65)   D'Elia, N. L.; Gravina, N.; Ruso, J. M.; Marco-Brown, J. L.; Sieben, J. M.; Messina, P. V. Albumin-Mediated
624   Deposition of Bone-like Apatite onto Nano-Sized Surfaces: Effect of Surface Reactivity and Interfacial
625   Hydration. *J. Colloid Interface Sci.* **2017**. https://doi.org/10.1016/j.jcis.2017.01.047.

626   (66)   Motta, A.; Migliaresi, C.; Lloyd, A. W.; Denyer, S. P.; Santin, M. Serum Protein Absorption on Silk Fibroin
627   Fibers and Films: Surface Opsonization and Binding Strength. *J. Bioact. Compat. Polym.* **2002**, *17* (1), 23–
628   35. https://doi.org/10.1177/0883911502017001195.

629   (67)   Mandal, B. B.; Gil, E. S.; Panilaitis, B.; Kaplan, D. L. Laminar Silk Scaffolds for Aligned Tissue Fabrication.
630   *Macromol. Biosci.* **2013**, *13* (1), 48–58. https://doi.org/10.1002/mabi.201200230.

631